Energy Engineering

Tech Science Press

https://doi.org/10.32604/ee.2025.076483

ARTICLE

Numerical Study on Operation Optimization of Low NOx Combustion Characteristics of Swirl Impact Gas Burner

Zhenjie Yuan, HaiLong Yu* and Hongjun Cao

School of Petroleum and Natural Gas Engineering, School of Energy, Changzhou University, Changzhou 213164, China

*Corresponding Author: HaiLong Yu. Email: yhl@cczu.edu.cn

Received: 21 November 2025; Accepted: 18 December 2025; Published: 12 November 2026

ABSTRACT: Low-NOx combustion of natural gas is essential for cleaner industrial heat supply under increasingly strict emission regulations. However, many existing low-NOx swirl burners still rely on single-mechanism control and suffer trade-offs between temperature suppression, combustion stability, and mixing uniformity. This work develops and numerically optimizes a structurally integrated cyclonic-impingement natural-gas burner that combines four rows of impinging secondary-air jets with four axially deflected main fuel nozzles, realizing a coupled swirl-impingement-staging mechanism that differs fundamentally from conventional swirl burners employing only geometric swirl or simple air staging. Validated three-dimensional RANS CFD simulations (realizable k-ε turbulence model, steady diffusion flamelet combustion, and DO radiation), after grid-independence testing and comparison with literature data, are used to quantify the effects of burner load, primary/secondary air ratio, excess air coefficient, and air-preheating temperature on the furnace thermal field, flow structures, and NOx distribution. The results show that the proposed burner maintains ultra-low-NOx operation with outlet concentrations below 50 mg·m^{-3} over the entire operating range, while preserving complete and stable combustion. A primary-to-secondary air ratio of 2:8 and an excess air coefficient of about 1.05 provide an optimal compromise between combustion intensity and emission control, and operation with approximately ambient-temperature air (≈300 K) is recommended when NOx reduction is prioritized. Within the investigated parameter space, the simulated NOx levels fall within or below the ranges reported for low-NOx swirl burners in the literature, while offering a structurally distinct solution based on integrated swirl-impingement-staging. These findings highlight the practical potential of the proposed integrated design as a compact ultra-low-NOx option for upgrading industrial gas-fired combustion systems to cleaner operation.

KEYWORDS: Swirl impact gas burner; ultra-low NOx emission; numerical simulation

1 Introduction

Burners are one of the most essential thermal elements within boiler systems, substantially influencing combustion efficiency and pollutant emissions [1]. Significant global attention has been drawn to improvements in burner technology. Recent studies emphasize natural gas as the primary fuel due to its high thermal efficiency and environmental advantages, particularly its ability to limit NOx formation and comply with strict emission regulations [2]. Current research prioritizes the design of advanced high-efficiency and low-emission combustion and gas-utilization configurations to enhance thermal efficiency, optimize combustion control mechanisms, and reduce emissions at the source [3–6]. Consequently, optimization of structural and operational parameters is critical in the development of modified burners, given the direct effects on industrial progress, economic sustainability, and environmental protection. Acceleration of fundamental research in low-NOx combustion technology remains an urgent priority within the scientific field [7].

Copyright © 2027 The Authors. Published by Tech Science Press. This work is licensed under a Creative Commons Attribution 4.0 International License, which permits unrestricted use, distribution, and reproduction in any medium, provided the original work is properly cited.

Li et al. [8] employed Large Eddy Simulations to investigate the effect of water vapor addition in partially premixed swirling ammonia/methane flames and showed that NO emissions can be reduced mainly through physical dilution; however, excessive addition leads to marked flame instability, revealing a trade-off between NOx abatement and stable operation. Zhien and Ali Al-attab [9] analyzed a cyclonic multi-stage combustor for low-grade biomass producer gas and demonstrated that high-temperature low-oxygen staging improves low-NOx performance, yet their configuration is closely tied to the specific fuel properties and does not explicitly address temperature uniformity in compact gas-fired systems. Lei et al. [10] numerically examined a gear-type combustion stabilizer in a swirl burner and reported a 17.02% reduction in NOx due to enhanced rich/lean separation, but the optimization remained limited to local stabilizer geometry without coordinated control of fuel–air staging or near-wall recirculation. Shao et al. [11] explored layered combustion of peanut-shell briquette fuel and identified an optimal primary air-supply rate for minimizing NOx, while the applicability of this strategy is largely confined to biomass-fired furnaces. Zeng et al. [12] combined experiments and simulations to clarify NOx formation and reduction mechanisms in stereo-staged pulverized-coal combustion, confirming the key role of air equivalence ratio but still revealing a tension between reduced peak temperatures and sufficient burnout. Huang et al. [13] proposed a water-cooled premixed natural-gas burner that lowers NOx emissions by decreasing furnace temperatures, although the associated efficiency penalty and structural complexity restrict its practical use. Taken together, these representative studies indicate that single-mechanism approaches—such as diluent addition, swirl modification, air or fuel staging, and external cooling—can suppress NOx under certain conditions, yet they also expose persistent trade-offs among temperature suppression, combustion stability, and mixing uniformity, and seldom treat swirl, staging, and recirculation as part of an integrated burner design.

The present study concentrates on the development and multi-objective optimization of a new low-NOx natural gas burner that integrates complementary emission-control strategies such as staged air supply, graded fuel distribution, and enhanced cyclonic flow to create a cyclonic impingement combustion configuration. Structurally, the combustor incorporates four rows of impinging secondary-air tubes, each row containing eight uniformly spaced jets to reinforce convective mixing across the furnace cross-section, while four main fuel pipes are equipped with burner nozzles that include a finite axial deflection to stabilize the flame and control the effective swirl intensity. In contrast to conventional swirl burners, this arrangement establishes a coupled "swirl-impingement-staging" mechanism, in which a tangential primary jet forms a concentrated vortex core that impinges on a concave flame-stabilizing surface before interacting with the staged secondary-air jets. Through this confined recirculation and multi-point mixing, fuel-air micro-mixing is intensified and high-temperature regions are more evenly redistributed in the main combustion zone, helping to alleviate local peak temperatures while maintaining stable low-NOx combustion. Three-dimensional computational fluid dynamics (CFD) simulations, performed using ANSYS FLUENT, were employed to quantitatively analyze temperature gradients, vortex-driven flow structures, and NOx spatial distributions within the combustion chamber. Through response surface-based multi-objective optimization, the study not only identifies structural and operational parameters that minimise NOx emissions but also demonstrates measurable improvements in stability and combustion efficiency compared with existing swirl-type low-NOx burners, thereby providing a clearly differentiated burner configuration with promising potential for practical deployment.

2 Method of Calculation

2.1 Physical Model

The combustion of natural gas with an oxidizing medium inside a combustion chamber represents a multifaceted physicochemical process that combines intricate mechanisms of heat transfer, fluid dynamics,

and mass as well as energy exchange. Consequently, several mathematical models are employed in this research to capture and represent the different physicochemical interactions involved.

2.1.1 Governing Equation

The flow analyzed in this study is governed by three primary conservation laws: the conservation of mass, the conservation of momentum, and the conservation of energy [14].

(1) Mass conservation equation:

$$\frac{\partial \rho}{\partial t} + \frac{\partial}{\partial x_j}\left(\rho u_j\right) = 0 \tag{1}$$

(2) Equation of conservation of momentum:

$$\frac{\partial}{\partial t}\left(\rho u_i\right) + \frac{\partial}{\partial x_j}\left(\rho u_i u_j\right) = -\frac{\partial P}{\partial x_i} + \frac{\partial}{\partial x_j}\left(\tau_{ij}\right) + \rho f_i \tag{2}$$

(3) Energy conservation equation:

$$\frac{\partial}{\partial x_i}\left(\rho C_P T\right) + \frac{\partial}{\partial x_j}\left(\rho C_P u_j T\right) = \frac{\partial}{\partial x_j}\left(\frac{\mu}{Pr}\lambda\frac{\partial C_P T}{\partial x_j}\right) + w_s Q_S \tag{3}$$

2.1.2 Viscous Model

In the present work, the turbulent flow in the combustor is described by the Reynolds-averaged Navier–Stokes (RANS) equations, and a turbulence closure is required to model the Reynolds stresses. Given the high Reynolds number, strong swirl and pronounced recirculation induced by the swirl–impingement configuration, the realizable k-ε model is adopted as a compromise between predictive accuracy and computational cost. This model has been reported to provide improved performance over the standard k-ε formulation for flows with strong streamline curvature and rotation, such as swirling jets and combustor internal flows [15]. In the present swirl impingement gas burner, the realizable k-ε model is therefore employed to capture the main features of the recirculation zones and shear layers while keeping the overall computational effort at a practically acceptable level.

2.1.3 Combustion Model

In the present work, combustion in the swirl impingement burner is treated as a non-premixed process and is described using a steady diffusion flamelet formulation within a Reynolds-averaged (RANS) framework. Within the flamelet concept, the thin reaction zone is treated as a quasi-laminar diffusion flame embedded in a turbulent flow field, and the thermo-chemical state is parameterized by the mixture fraction and its scalar dissipation rate [16]. The mixture fraction Z is constructed from the elemental mass fractions of the fuel, oxidiser and products according to Eq. (4), and the local equivalence ratio ϕ is obtained from Z using Eq. (5).

$$Z = \frac{\beta - \beta_{ox}}{\beta_f - \beta_{ox}} \tag{4}$$

$$\phi = \frac{Z/(1-Z)}{Z_{st}/(1-Z_{st})} \tag{5}$$

$$\beta = Z_C + \frac{Z_H}{4} + \frac{Z_N}{2} \tag{6}$$

To retain computational efficiency, a library of adiabatic, steady counter-flow diffusion flamelets is pre-computed with detailed (or reduced) chemistry, and the species mass fractions and source terms are subsequently obtained by interpolation in this library during the CFD simulation [17]. Although radiative and convective heat losses can alter the absolute temperature level, their influence on the normalized species profiles is assumed to be moderate, so the use of an adiabatic flamelet library represents a commonly adopted engineering approximation for furnace-scale simulations. The combustor investigated here features multiple fuel and oxidiser inlets and predominantly non-premixed mixing; under these conditions, the steady diffusion flamelet model provides a reasonable compromise between physical fidelity and computational cost and is adequate for predicting the main trends of furnace temperature and NOx formation.

2.1.4 Radiation Model

The heat exchange between the flame and the furnace heating components requires the use of an appropriate radiative heat-transfer model to ensure accurate simulation outcomes. The Fluent software provides several radiation models, including the discrete transfer radiation model, the Rosseland approximation, and the discrete ordinates formulation [18]. Considering the participating gaseous medium, the complex surface-to-surface energy exchange and the need to balance accuracy with computational cost, the DO model is adopted in this study to describe radiative heat transfer within the combustion simulations.

2.2 Burner Structure

Swirl impact gas burners are modified versions of conventional combustion devices that are widely investigated as low-NOx combustion systems and can achieve reduced NOx levels in the exhaust compared with standard swirl burners. Their functioning relies on specially contoured internal aerodynamic passages that create swirling flows, promoting thorough mixing of fuel and oxidizer and ensuring even distribution, which in turn improves combustion performance. Drawing on key principles of ultra-low-NOx (ULN) combustion—such as staged air supply and enhanced internal recirculation—an initial configuration of the present burner was designed, and its three-dimensional geometry is illustrated in Fig. 1.

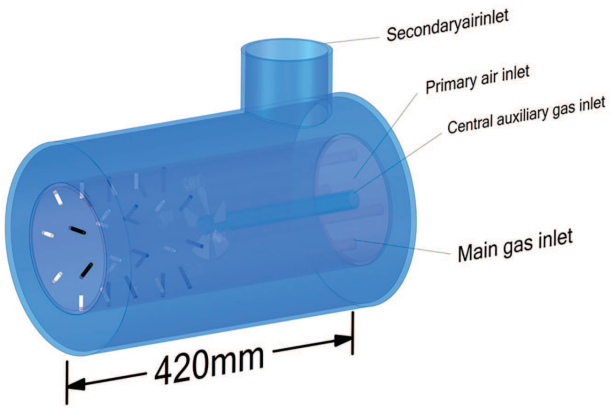


Figure 1: Structure of a swirl impact gas burner

As shown in Fig. 1, the cyclonic impingement burner consists of a central primary fuel duct, annular air passages, fuel distribution manifolds with multi-orifice gas injectors, and swirl vanes. The central fuel duct

is positioned on the burner axis and is designed for outward radial fuel injection into the surrounding air stream. Each surrounding gas manifold is equipped with a multi-orifice injector that features a central main jet encircled by four smaller jets responsible for flame stabilization. The secondary air system is arranged as eight vertically aligned ducts, paired axially with identical dimensions and evenly distributed around the burner circumference. These ducts are positioned along the inner wall within an annular plenum that also provides convective cooling of the duct walls. Both oxidizer and fuel are introduced in two distinct stages. Controlled staging of the air supply is a key mechanism for achieving efficient and clean combustion, while the small-scale secondary ducts act as stability regulators, helping to lower pollutant emissions by separating pyrolytic and oxidative reaction regions within the flame.

The intricate structure of the burner demands substantial computational resources. Preliminary simulations with extended furnace lengths (not shown) indicated that the downstream section has a negligible influence on the near-burner flow and temperature fields. Therefore, the present analysis focuses on the truncated upstream portion of the cyclonic impingement burner, which was simplified for computational modeling.

A two-dimensional schematic of the simplified swirl impact gas burner is illustrated in Fig. 2, while Table 1 provides its detailed dimensional specifications. Following the development of the simplified combustor model, the chamber design was adjusted accordingly. Based on the dimensions of the radiant section of the boiler, the chamber was configured with a length of 1000 mm and a diameter of 500 mm.

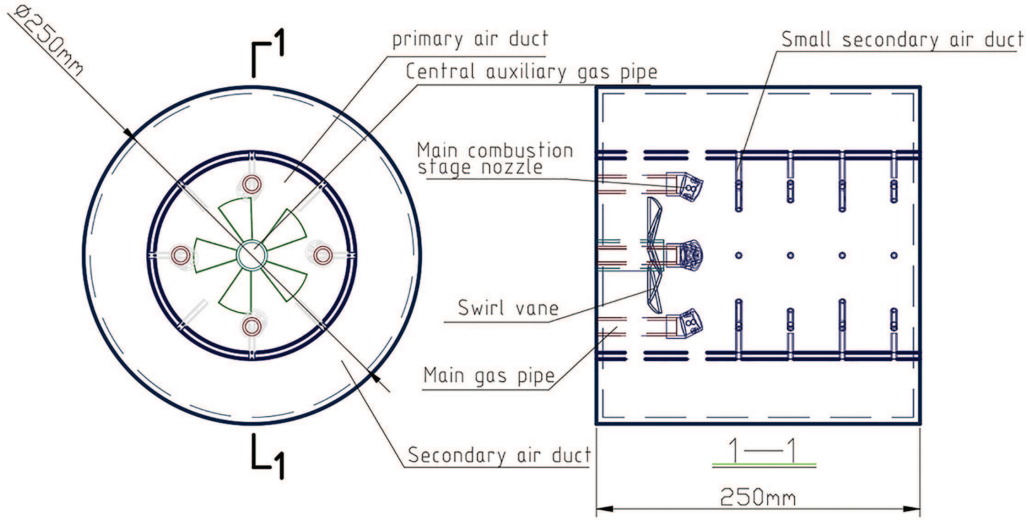


Figure 2: Two-dimensional schematic of a swirl impact gas burner

Table 1: Simplified structural dimensions of a cyclone impingement gas burner

Name	Unit	Size
Overall length of combustor	mm	420
Diameter of combustor	mm	250
Length of main gas pipe	mm	60
Diameter of main gas pipe	mm	10
Length of secondary gas pipe	mm	50
Diameter of secondary gas pipe	mm	20

(Continued)

Table 1 (continued)

Name	Unit	Size
Diameter of primary air duct	mm	150
Diameter of secondary air small duct	mm	3.8
Number of cyclone blades	Number	5
Cyclone blade angle	Degree	20

2.3 Computational Grid

Fig. 3 illustrates the integration of the swirl impact gas burner with the furnace chamber. The simplified representation of the burner is discretized through tetrahedral meshing, and mesh refinement is applied to regions of the burner where structural complexity is significant. In contrast, the furnace chamber possesses a relatively simple geometry, which allows it to be divided using structured meshing. The two separate mesh systems are linked together through an INTERFACE face.

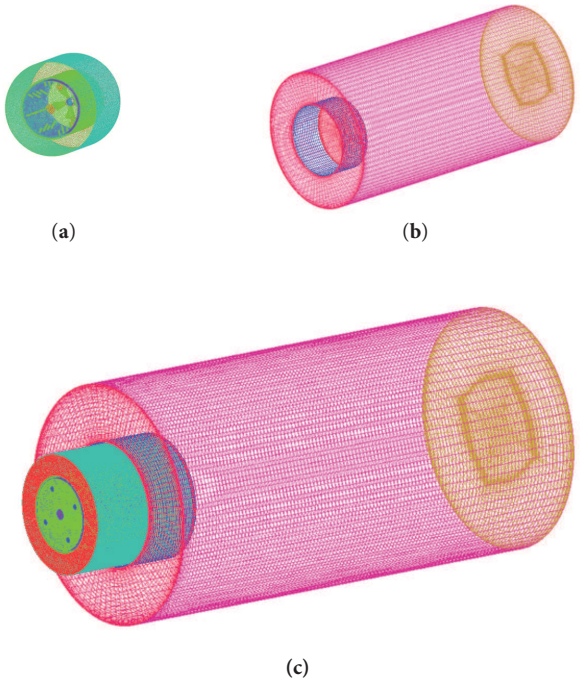


Figure 3: Computational domain grid. (**a**) Swirl impact burner, (**b**) Furnace, (**c**) Swirl impact burner and Furnace

2.4 Boundary Condition

For the design calculations presented in this study, a burner with a rated capacity of 700 kW is selected, and its principal technical specifications are listed as follows.

Rated output for the low nitrogen burner: 700 kW.

Energy source: natural gas.

Heating value of natural gas: 8600 kcal/m^3.

Heat load:

$$q_v = 700 \times 860 = 6.02 \times 10^5 \text{ kcal} \tag{7}$$

Gas consumption:

$$Q = 6.02 \times 10^5 / 8600 = 70\,m^3/h \tag{8}$$

In the present work, an excess air coefficient of 1.05 was applied, corresponding to a calculated combustion gas demand of 9.996 m^3. Although industrial natural gas typically consists of multiple components, the numerical model considered methane as the sole fuel species to simplify the calculation process. The oxidizing medium was defined as a binary mixture of oxygen and nitrogen, with inlet temperatures for all streams fixed at 26.85°C. The specified excess air coefficient was maintained throughout the simulation.

NOx concentration can be calculated using the following expression:

$$C_{NO_x} = \rho_{out} Y_{NO_x,out} \times 10^6 \tag{9}$$

In this expression, C_{NO_x} is the NOx mass concentration on a dry or wet basis at the furnace outlet, ρ_{out} represents the actual density of the flue gas at the furnace outlet, and $Y_{NO_x,out}$ denotes the mass fraction of NOx component in flue gas at the furnace outlet.

In this study, NOx concentrations are expressed as outlet flue-gas mass concentrations ($mg \cdot m^{-3}$, wet basis) without normalization to a reference oxygen level, unless otherwise specified.

In the numerical modeling carried out for this study, the inlet flow rate is derived from the burner's operational specifications. The wall temperature of the burner is maintained at a constant 500 K, while the furnace chamber wall is set at a fixed 1000 K. Details of the boundary condition settings are provided in Table 2.

Table 2: Boundary conditions

Name	Diameter (mm)	Velocity (m/s)
Entrance-main gas	10	55.82
Entrance-primary air	150	2.36
Entrance-subgas	20	6.24
Inlet-secondary air	250	5.41
pressure outlet	500	

2.5 Solver Settings

The simulations were performed using the pressure-based segregated solver in ANSYS FLUENT. For pressure-velocity coupling, the SIMPLE algorithm was adopted, as the present problem is treated as statistically steady and preliminary tests indicated no appreciable differences in the mean flow and temperature fields when compared with SIMPLEC, while SIMPLE provided slightly more robust convergence [19]. The pressure equation was discretized using the standard scheme, and gradients were computed with the Green-Gauss cell-based method. All convective terms in the momentum, turbulence, species and energy equations were discretized with a second-order upwind scheme to reduce numerical diffusion.

Under-relaxation factors were chosen based on both FLUENT default settings and additional convergence tests. The default values were retained for pressure, density and turbulent kinetic energy, whereas the

momentum under-relaxation factor was set to 0.5 to stabilize the solution in regions with strong recirculation. For species, a value of 0.8–0.9 was found to offer a good compromise between stability and convergence rate; for the energy and radiation equations, an under-relaxation factor of 0.9 was used [20]. During the iterative process, residuals of all equations were monitored and reduced below 10^{-4} (10^{-6} for the energy equation), and global quantities such as furnace outlet temperature and average NOx concentration were required to reach steady values before a solution was accepted as converged.

To improve robustness, a two-step solution procedure was employed. First, an isothermal "cold-flow" simulation was carried out by solving only the flow and turbulence equations until a steady recirculating velocity field was obtained. Subsequently, the energy, radiation and species transport equations were activated, and iterations were continued until both residual and integral convergence criteria were satisfied.

2.6 Grid Independence and Boundary-Layer Velocity Profiles

To verify that grid quantity does not influence the accuracy of the simulation, numerical tests were conducted with grid schemes A through F under identical operating conditions. The corresponding outcomes are presented in Table 3 and Fig. 4. From grid D onward, the temperature fluctuations become stable. Taking into account the computational capacity available, grid D is selected for use in this study.

Table 3: Grid-independent relevance verification

	A	B	C	D	E	F
Number of grids (millions)	65	108	137	196	270	320
Average outlet temperature (K)	418.136	440.114	488.707	408.231	407.076	408.039
Maximum furnace chamber temperature (K)	2243.046	2210.924	2185.194	2024.877	2013.123	1971.529
Furnace average velocity (m/s)	24.040	25.306	26.620	27.284	27.195	27.800

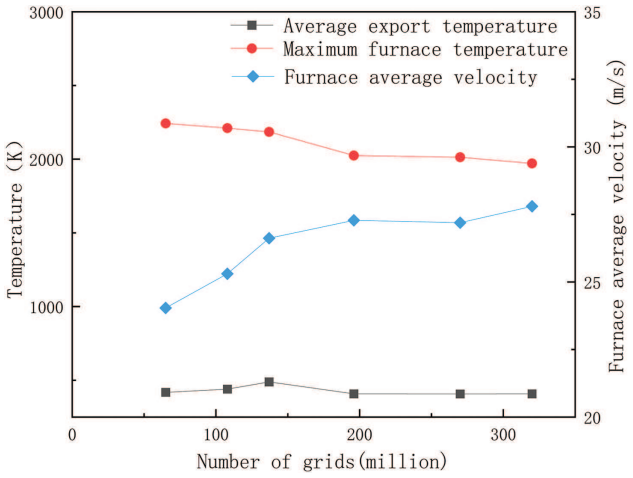


Figure 4: Distribution of average outlet temperature, maximum furnace temperature, and average furnace velocity with different grids

In addition to the grid independence study, the non-dimensional wall distance (y^+) is a key metric for evaluating near-wall mesh quality. It quantifies the distance from the wall in boundary layer flows and is

crucial for accurately resolving turbulent structures and wall shear effects. y^+ is defined as [21]:

$$y^+ = \frac{u_\tau \Delta y}{\nu} \tag{10}$$

where Δy is the distance from the wall to the center of the first computational cell, $u_\tau = \sqrt{\tau_w/\rho}$ is the friction velocity derived from wall shear stress τ_w, and ν is the kinematic viscosity.

For wall-function-based Reynolds-averaged turbulence modeling, it is generally desirable that the first-cell center lies in the logarithmic region of the boundary layer (i.e., y^+ of the order of $10–10^2$), so that the empirical wall functions remain valid and the main near-wall momentum and heat-transfer trends are captured with acceptable accuracy. In the present mesh, excluding a small local peak near a geometric corner, the evaluated y^+ values on the burner and furnace walls lie between approximately 2.4 and 114, with an average of about 21; roughly three-quarters of the wall-adjacent locations fall in the range $y^+ = 5–30$, while only a few regions are slightly below 5 or above 30. This distribution indicates that the near-wall resolution is of the correct order of magnitude for the chosen realizable k-ε model with standard wall functions and is sufficient to represent the overall wall shear stress, heat-transfer behavior, and near-wall flow structures in the present simulations, while maintaining reasonable computational cost.

To complement the y^+ analysis, boundary-layer velocity profiles were extracted to further assess the near-wall resolution and verify that the wall-bounded flow is properly captured. Fig. 5 presents the non-dimensional streamwise velocity u/U_{bulk} as a function of the normalized radial coordinate y/R at three representative wall-normal sampling ranges, corresponding to the outer 20% of the radius ($0.80 \le y/R \le 1.00$), the outer half of the radius ($0.50 \le y/R \le 1.00$) and the full cross-section ($0 \le y/R \le 1.00$). For each case, profiles are shown at three axial locations downstream of the burner exit (z = 603, 840, 1077 mm), which characterize the evolution of the boundary layer along the combustor wall. Near the wall, all profiles converge to $u/U_{bulk} \to 0$ at y/R = 1, satisfying the no-slip condition and displaying steep velocity gradients that are well resolved by the current mesh.

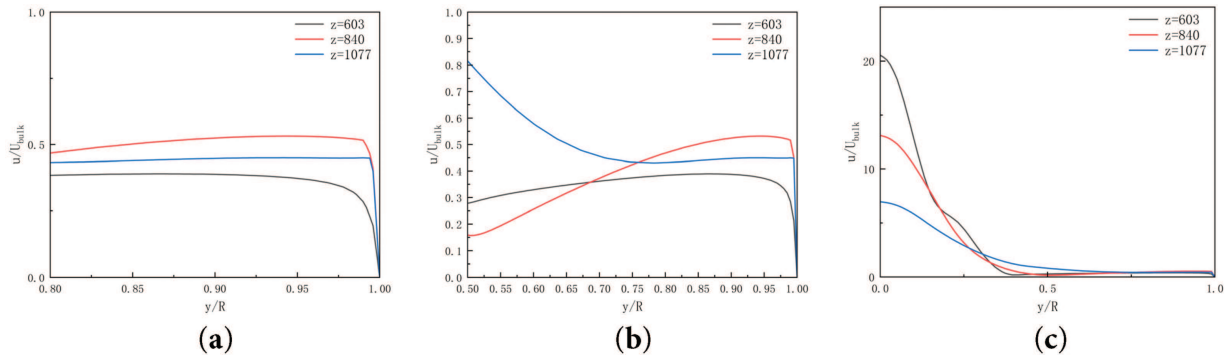


Figure 5: Boundary-layer velocity profiles of the streamwise velocity normalized by the bulk velocity, u/U_{bulk} at different axial positions z along the combustor. (**a**) Outer 20% of the radius ($0.80 \le y/R \le 1.00$), (**b**) outer half of the radius ($0.50 \le y/R \le 1.00$), (**c**) full radius ($0 \le y/R \le 1.00$)

In the outer 20% of the radius (Fig. 5a), the velocity remains significantly lower than the bulk value ($u/U_{bulk} < 1$), indicating a low-speed annular region associated with the turbulent boundary layer. As the flow progresses downstream, the near-wall velocity deficit expands toward smaller y/R, reflecting a gradual thickening of the boundary layer. When the sampling range is extended to the outer half of the radius (Fig. 5b), the profiles exhibit a smooth transition from the low-velocity near-wall region to the higher-velocity core, and the crossover of the curves at different axial positions reveals the decay of the central jet and

redistribution of momentum toward the outer shear layer. The full-radius profiles (Fig. 5c) further confirm that the jet-like core region close to the burner exit initially reaches peak velocities exceeding $20U_{bulk}$, but this excess momentum rapidly diminishes with increasing axial distance, while the near-wall region remains characterized by a monotonic decrease in u/U_{bulk} toward zero. These observations are consistent with the expected development of a turbulent boundary layer in a confined swirling jet and, together with the y^+ statistics, demonstrate that the near-wall flow is captured with sufficient accuracy for the present simulations.

2.7 Model Validation

The simulation results were compared with measurement data reported in a related study [22] to confirm the reliability of the selected numerical approach. Table 4 provides the inlet velocities of the burner corresponding to various load conditions. To ensure consistent boundary settings, the burner inlet velocities in the simulations were configured to match the operating parameters documented in [22] for each load case, and the same fuel type and nominal heat-load range were adopted as in the reference experiment.

Table 4: Burner inlet velocities under different load conditions

Scheme	Load	One wind speed (m/s)	Secondary wind speed (m/s)	Main combustion speed (m/s)	Secondary combustion speed (m/s)
1	f1	0.47	1.08	11.16	1.25
2	f2	0.94	2.16	22.33	2.50
3	f3	1.42	3.25	33.49	3.75
4	f4	1.89	4.33	44.66	5.00
5	f5	2.36	5.41	55.82	6.24

Fig. 6 compares the literature data and the simulated results of average furnace temperature, flow velocity, and NOx emission concentration across five different loads. The predicted average temperatures (1337.2–1460.7 K) closely match the values reported in [22] (1334–1455 K), with a maximum deviation of less than 0.6%. Similarly, the simulated average velocities (29.3–126.4 $m{\cdot}s^{-1}$) agree well with the literature values (29–125 $m{\cdot}s^{-1}$), showing consistent trends and magnitudes throughout. In terms of pollutant emission, both simulated and reported NOx concentrations rise steadily with increasing load. At load f1, the NOx concentrations given in [22] and the simulation are 18.36 and 18.74 $mg{\cdot}m^{-3}$, respectively, while at load f5 the values increase to 46.33 and 47.45 $mg{\cdot}m^{-3}$. The overall NOx prediction maintains a maximum relative deviation below 2.5% and an average deviation under 1.6%. Together with the mesh-independence study and the near-wall boundary-layer checks presented in Section 2.6, this close agreement for temperature, velocity and NOx across multiple operating conditions indicates that the present CFD model can reliably capture the coupled effects of flow, heat transfer and emission formation in this class of natural-gas burners. Although no independent experiments are currently available for the newly proposed swirl impact gas burner, the validated numerical framework from this benchmark configuration provides reasonable confidence for the subsequent parametric analysis and optimization of the new design.

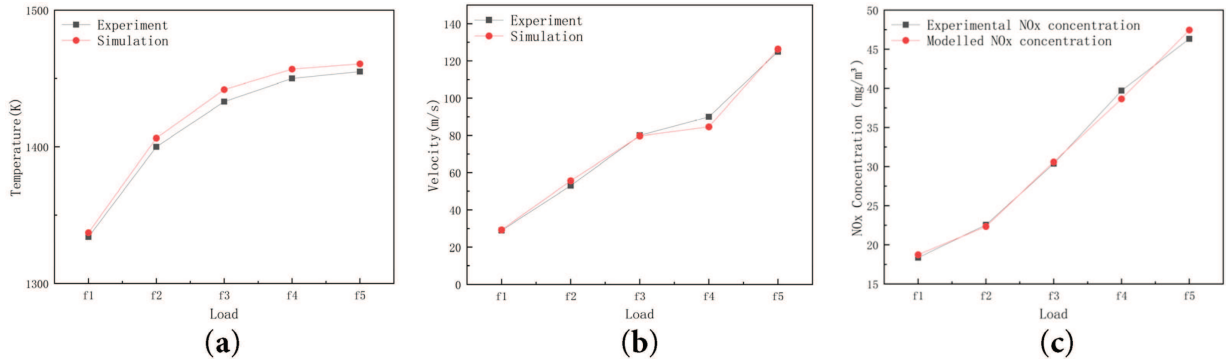


Figure 6: Comparison between the present simulation and experimental data from Ref. [22] under different loads. (**a**) Average furnace temperature, (**b**) Furnace average velocity, (**c**) Exhaust NOx emission concentration

3 Results and Discussion

3.1 Influence of Load

3.1.1 Temperature Field Analysis

Figs. 7 and 8 illustrate the temperature distribution within the burner at different loads and the temperature profile along the centerline, respectively. As the firing load increases, the high-temperature zone in the furnace chamber gradually extends downstream and occupies a larger cross-sectional area. Because only about 10% of the total fuel is injected through the central nozzle and the remaining 90% is supplied by the outer main gas pipes, the main flame is confined to the annular region of the furnace, and the temperature along the centerline remains lower than that near the periphery. This behavior is further influenced by the internal burner geometry: four rows of impinging secondary-air tubes, each row containing eight evenly distributed jets, and four main fuel pipes equipped with burner nozzles deflected by 30° in the axial direction. The impinging secondary jets and the deflected main nozzles enhance swirl and cross-stream mixing, driving the reaction zone towards the outer ring while maintaining a relatively cooler, recirculating core. The furnace exit, positioned at the right rear, allows flue gas to accumulate and form a reflux, which mixes hot products with cooler gases, moderates the local peak temperature, and consequently reduces nitrogen oxide emissions.

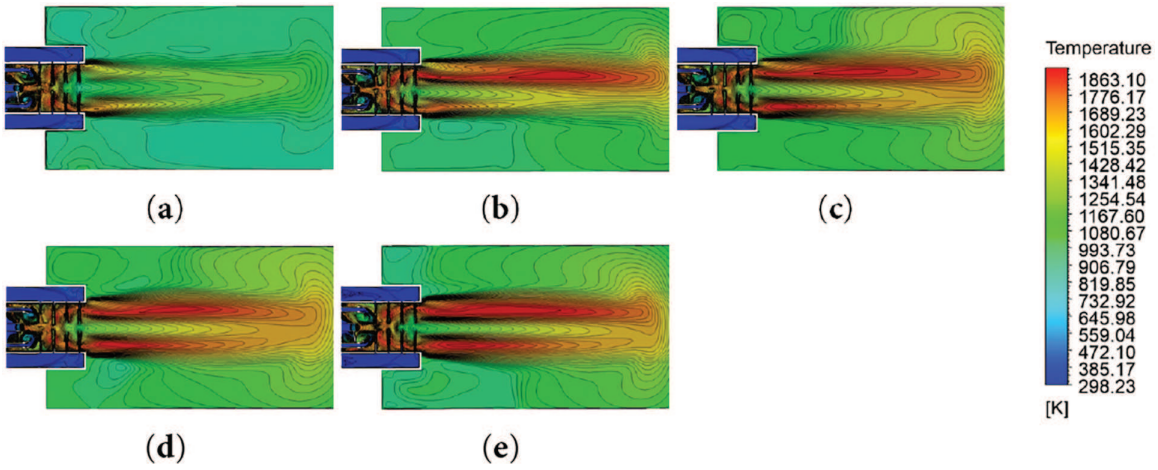


Figure 7: Temperature contours at the YZ section under different loads. (**a**) f1, (**b**) f2, (**c**) f3, (**d**) f4, (**e**) f5

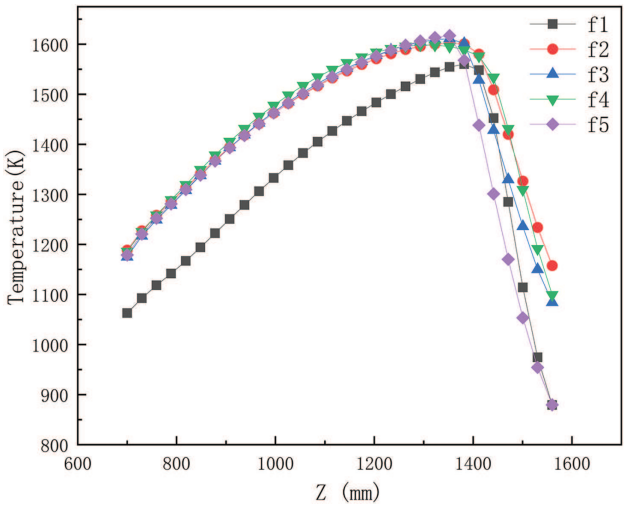


Figure 8: Axial temperature profiles under different loads

Figs. 7 and 8 indicate that as the load rises from f1 to f5, the centerline temperature and the temperature at the furnace outlet both increase, and the high-temperature region becomes more pronounced. The average temperature on the Y-Z section rises from 1168.5 to 1213.7 K, corresponding to an increase of about 45 K (≈5%). The furnace outlet exhibits a temperature range of 1000 to 1600 K, showing that combustion flue gas temperatures grow with increasing load.

3.1.2 Flow Field Analysis

The furnace chamber features a trapezoidal design with the outlet positioned at the side and rear. To examine internal flow patterns, the central longitudinal section YZ was selected for analysis, as depicted in Fig. 9. As the combustion load rises from f1 to f5, both gas and air flow rates increase, resulting in an overall upward trend in velocity across the central cross-section. Fig. 10 shows that velocity gradually decreases along the center axis of the chamber, with most flue gas exiting through the outlet while some forms a backflow in the central region. At a given axial position, the velocity field exhibits higher speeds near the burner axis and lower speeds close to the outer ring, reflecting the combined action of the central jet from the 30°-deflected main fuel nozzles and the multiple impinging secondary-air jets. The four rows of impinging secondary-air tubes generate strong shear layers and local recirculation zones, which intensify turbulent mixing between natural gas and air and help to stabilize the flame under all load conditions, leading to more complete combustion.

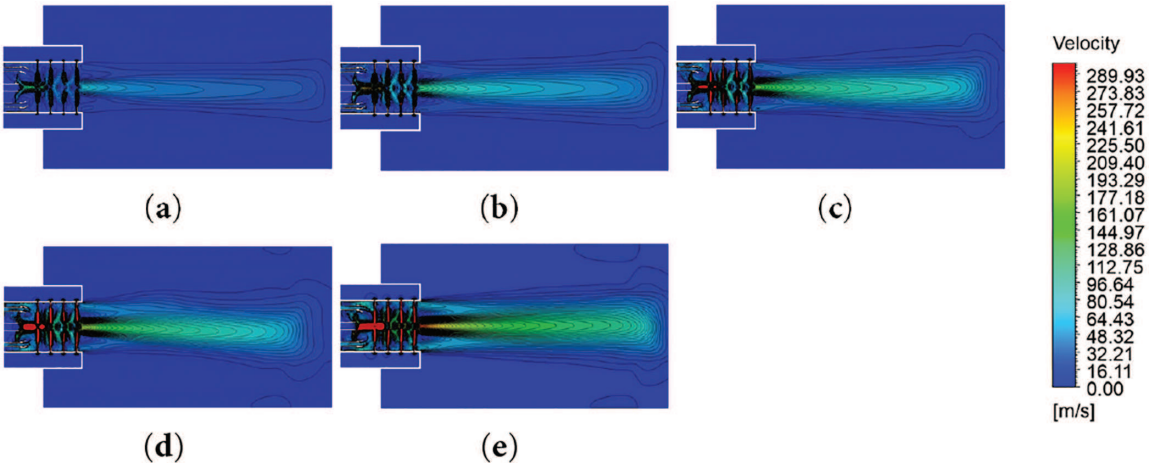


Figure 9: Velocity contours at the YZ section under different loads. (**a**) f1, (**b**) f2, (**c**) f3, (**d**) f4, (**e**) f5

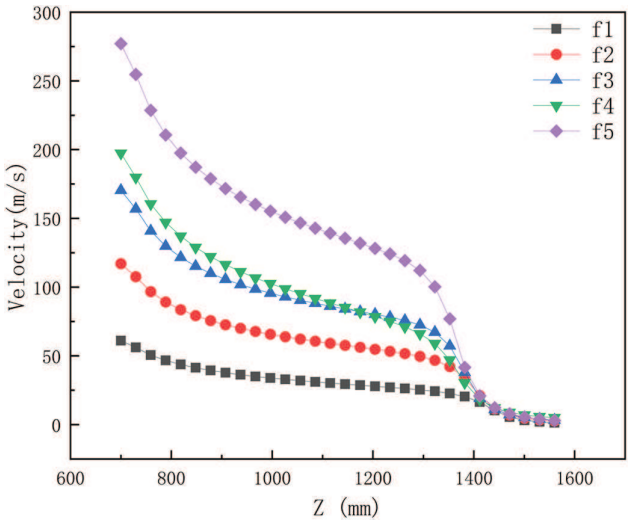


Figure 10: Axial velocity profiles under different loads

3.1.3 NOx Concentration Analysis

Fig. 11 presents the NOx distribution in the YZ plane under varying load conditions. Consistent with prior analyzes, NOx concentrations increase monotonically as the load rises from f1 to f5. As illustrated in Fig. 12, when the load is raised from f1 to f5, the combustion chamber temperature increases from 1168.51 to 1213.73 K, accompanied by a corresponding increase in NOx concentration from 18.74 to 47.45 mg·m^{-3}, remaining below the regulatory limit of 50 mg·m^{-3}. This trend reflects the strong sensitivity of thermal NOx formation to peak flame temperature. At the same time, the staged supply of fuel and air through the four axially deflected main fuel nozzles and the four rows of impinging secondary-air tubes promotes distributed combustion and effective flue-gas recirculation, which suppress local temperature spikes and enables the burner to maintain NOx emissions below the limit even at the highest load. These results indicate that combustion load exerts a notable influence on both furnace temperature and NOx emissions, while the specific cyclonic-impingement burner structure plays a key role in limiting NOx under high-load operation.

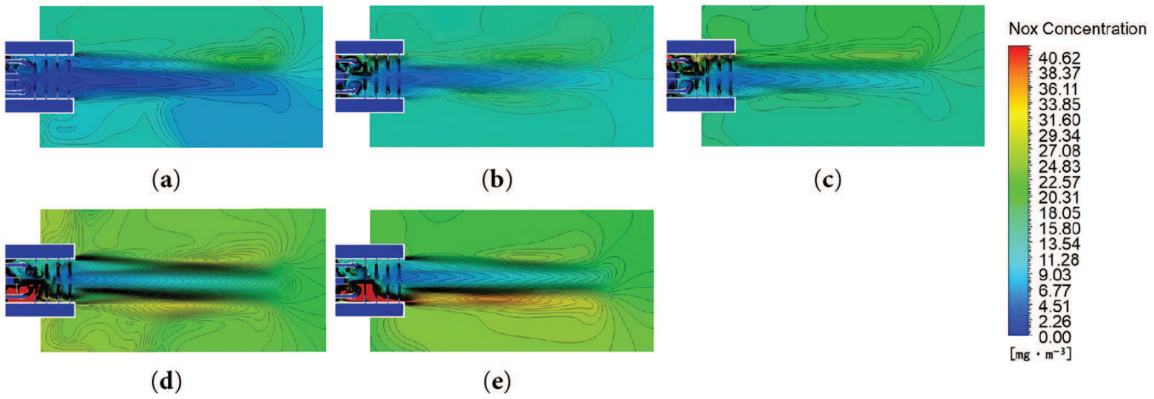


Figure 11: NOx concentration contours at the YZ section under various loads. (**a**) f1, (**b**) f2, (**c**) f3, (**d**) f4, (**e**) f5

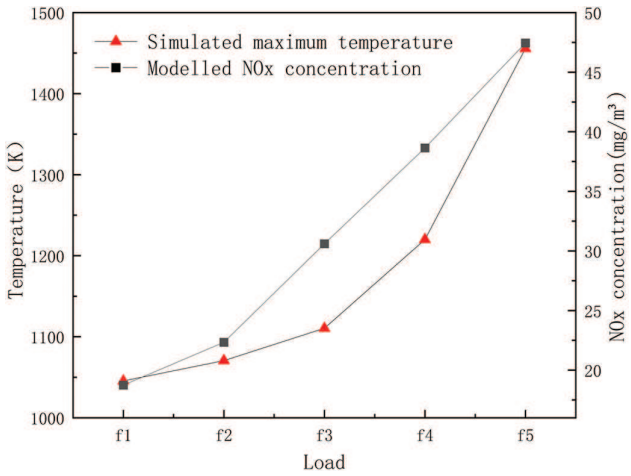


Figure 12: NOx concentration and maximum temperature profiles under different loads

3.2 Influence of Primary-to-Secondary Air Ratio

The operating conditions of the swirl impact gas burner play a crucial role in NOx formation. This section explores the influence of variations in primary-to-secondary air ratios on the low-NOx combustion performance of the burner. Simulations were conducted using default parameters: full-load operation, a swirl vane deflection angle of 20°, four main-stage combustion nozzle holes, an excess air coefficient of 1.05, and an air preheating temperature of 300 K. On this basis, three primary-to-secondary air ratios were investigated, namely 1:9, 2:8 and 3:7, by analyzing the resulting temperature fields, flow structures and NOx distribution patterns.

Fig. 13 illustrates the temperature distribution for three primary-to-secondary air ratios. Among the three cases, the 2:8 primary-to-secondary air ratio produces the most favorable temperature field, with a well-developed high-temperature core and relatively smooth axial decay. At this configuration, the larger share of secondary air interacts with the flame downstream of the burner exit, enhancing contact between fuel and oxidiser and promoting more complete combustion while avoiding excessively oxygen-rich or over-diluted zones near the burner head; as a result, peak temperatures are moderated and thermal NOx formation is constrained. When the primary-to-secondary ratio is reduced to 1:9, the small amount of primary air may lead to weaker near-nozzle jet momentum and less intense initial fuel–air mixing, which in practice could result in poorer ignition robustness and a lower overall furnace temperature. Increasing the primary air

fraction strengthens the central jet and raises the local oxygen concentration, which accelerates combustion and elevates the overall flame temperature; however, an excessively large primary share (3:7) tends to push the reaction zone away from the burner axis and makes the temperature field more non-uniform, indicating a greater risk of unstable combustion and local hot spots.

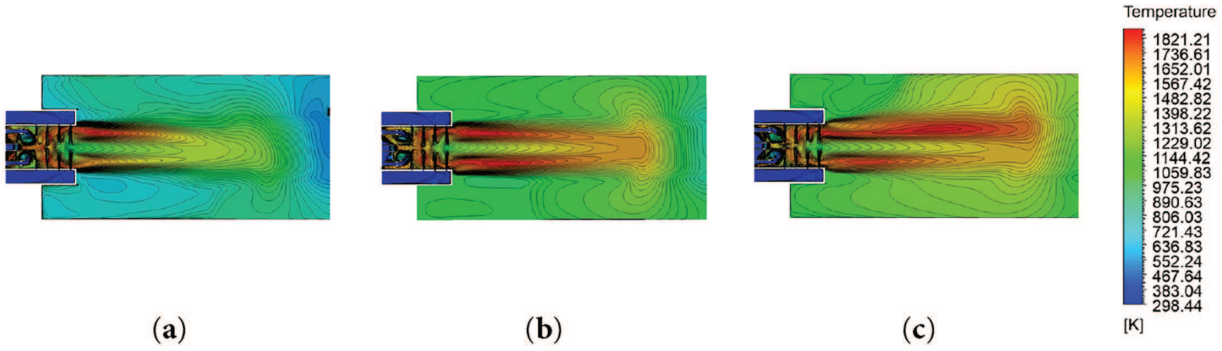


Figure 13: Temperature contours for different primary-to-secondary air ratios. (**a**) primary-to-secondary air ratio 1:9, (**b**) primary-to-secondary air ratio 2:8, (**c**) primary-to-secondary air ratio 3:7

Fig. 14 presents the average temperature distributions across different planes for varying primary-to-secondary air ratios. At a ratio of 1:9, the dominance of secondary air produces strong local vortices near the burner head and steep temperature gradients in the near-burner region. In contrast, the 3:7 case exhibits a noticeably lower peak temperature in the core because of stronger near-axis penetration of the primary jet and enhanced dilution of the flame by excess air. For the 2:8 case, the cyclone strength and mixing efficiency are better balanced, and the oxygen concentration boundary layer is closely aligned with the reaction zone, which reduces axial temperature fluctuations and yields a more uniform temperature field throughout the furnace. These results indicate that allocating 80% of the air as secondary flow provides a favorable compromise between oxygen transport and turbulent mixing, leading to an improved temperature distribution in the combustion chamber.

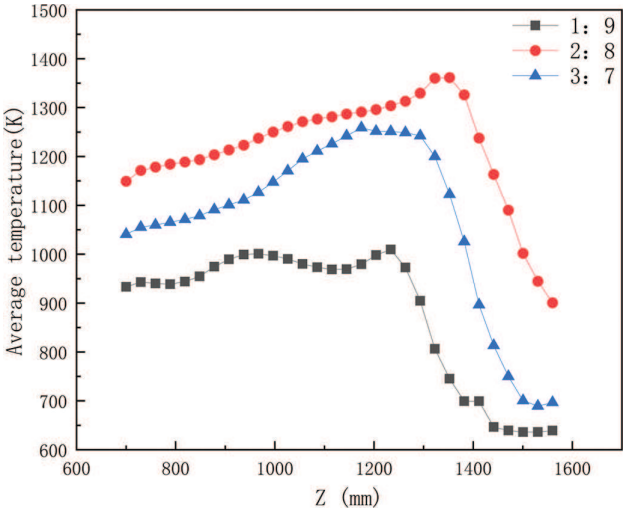


Figure 14: Mean temperature profiles of each plane for various primary-to-secondary air ratios

Fig. 15 presents the velocity contours corresponding to three different primary-to-secondary air ratios. In all cases, the highest flow velocity occurs near the junction between the burner outlet and the small secondary-air duct outlets. It is observed that when the primary-to-secondary air ratio reaches 2:8, the flow stabilizes, while further increasing the ratio to 3:7 causes the combustion to shift away from the *Z*-axis. Supplying 20% primary air provides sufficient initial momentum for the fuel jet and maintains a stable conical flame, whereas 80% secondary air is injected in multiple stages, forming an enhanced mixing region in which the interaction between the main jet and the impinging secondary jets promotes vigorous yet controlled turbulence. The large proportion of secondary air also generates a recirculation zone around the main jet that increases the residence time of partially reacted gases in the combustion zone and improves burnout; owing to the staged injection and distributed mixing, this enhanced recirculation does not lead to excessively high peak temperatures and is therefore beneficial for both combustion efficiency and NOx control. Fig. 16 illustrates the velocity profiles at z = 257 mm for the first two air ratios. As the primary-to-secondary air ratio increases, the central velocity decreases, and the high-velocity region expands, promoting improved mixing between intermediate fuel and air.

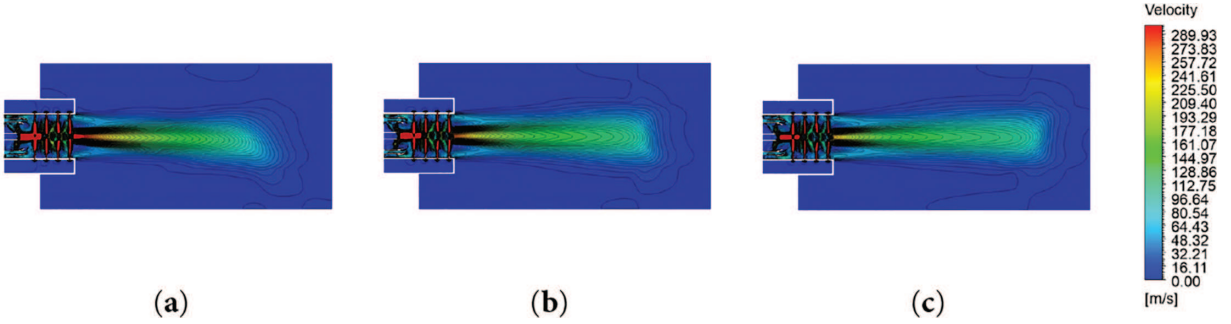


Figure 15: Velocity contours under various ratios of primary and secondary air. (**a**) primary-to-secondary air ratio 1:9, (**b**) primary-to-secondary air ratio 2:8, (**c**) primary-to-secondary air ratio 3:7

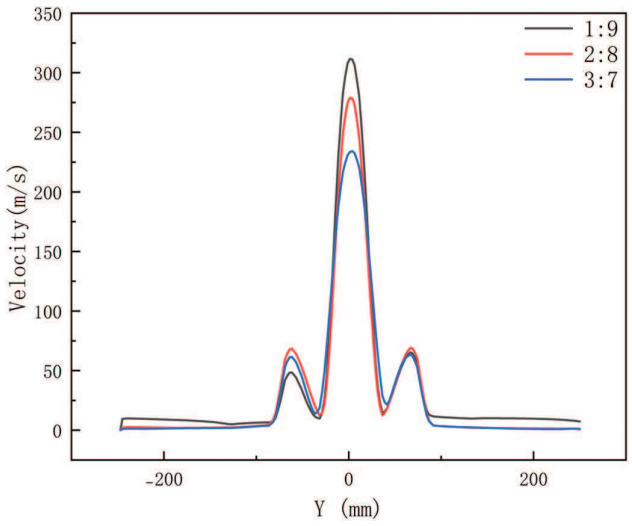


Figure 16: Velocity distribution curves for different primary and secondary air distribution ratios at interface z = 257 mm

Fig. 17 presents the nitrogen oxide concentration distribution under varying primary-to-secondary air ratios. Simulation results indicate that increasing the proportion of primary air leads to higher NOx concentrations. The minimum NOx level is obtained for the 1:9 case (10% primary air and 90% secondary air), where the relatively low furnace temperature suppresses thermal NO formation but also corresponds to a comparatively low heat-release level. When the secondary-air share is reduced to 70% (3:7), the higher flame temperature and more oxygen-rich core produce clearly increased NOx emissions. Balancing combustion efficiency and pollutant emissions, the optimal primary-to-secondary air ratio is determined to be 2:8.

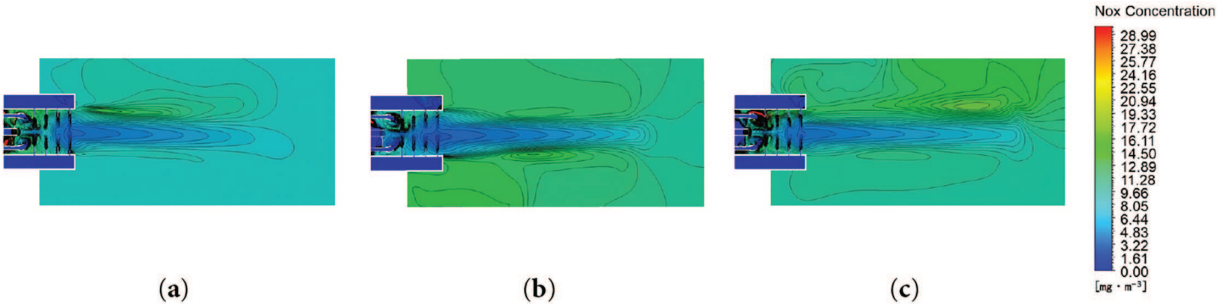


Figure 17: NOx concentration contours under various primary-to-secondary air ratios. (**a**) primary-to-secondary air ratio 1:9, (**b**) primary-to-secondary air ratio 2:8, (**c**) primary-to-secondary air ratio 3:7

3.3 Influence of the Excess Air Coefficient

To examine the influence of the excess air coefficient on low-NOx combustion performance in the swirl impact gas burner, a series of simulation conditions was established. The burner operates at full load, with the swirler vane fixed at a 20° deflection angle and four nozzles in the main combustion stage. The primary-to-secondary air ratio is set at 2:8, and the air preheating temperature is 300 K. Under these baseline conditions, four excess air coefficients were considered, α = 1.03, 1.05, 1.07 and 1.09, and their effects on temperature distribution, flow characteristics and NOx emission patterns were evaluated.

Fig. 18 presents the temperature distribution for various excess air coefficients. The results show that as the excess air coefficient rises, the average furnace temperature first increases and then decreases, while the flame structure remains largely unchanged. Increasing the coefficient from 1.03 to 1.05 promotes more complete combustion, enhances heat release, and raises the furnace temperature. Further increasing the coefficient from 1.05 to 1.09 introduces cooler air into the chamber, reducing the overall temperature generated by combustion.

Figs. 19 and 20 illustrate the velocity contours and velocity profiles at the z = 257 mm interface for different excess air coefficients. As the excess air coefficient increases, the overall flow velocity within the combustion chamber rises and the radial extent of the high-velocity region becomes larger. At the same time, the decay of swirl along the axial direction slows down and the turbulence intensity in the core jet increases, indicating stronger momentum exchange between the primary and secondary streams. For the largest excess air coefficient (α = 1.09), the balance between jet impingement momentum and secondary-air injection is disturbed, and the velocity distribution becomes more uneven, suggesting enhanced dynamic pressure fluctuations and a greater likelihood of local flow instabilities.

Fig. 21 presents the NOx concentration distribution for various excess air coefficients. It is observed that the NOx levels in the swirl impact gas burner display a non-monotonic trend, initially decreasing and then rising. The lowest NOx concentration occurs at an excess air coefficient of 1.05, where the combination of sufficient oxygen supply and relatively moderate peak temperatures yields a more favorable balance between

combustion completeness and thermal NO formation. At lower excess air (α = 1.03), local near-stoichiometric high-temperature zones can still develop because of limited mixing, which maintains significant thermal NOx production despite the lower global air ratio. When α is increased beyond 1.05, the additional oxygen and the extended residence of gases in moderately high-temperature regions promote the classical thermal NOx mechanism via the Zeldovich route [23], leading to a gradual increase in NOx emissions. Overall, these results indicate that an excess air coefficient of about 1.05 offers the best compromise between combustion performance and NOx control for the present burner configuration.

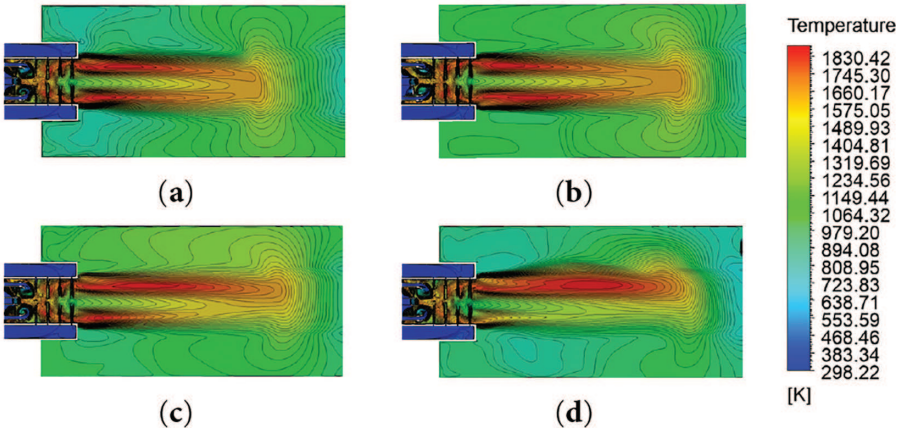


Figure 18: Temperature contours across different excess air coefficients. (**a**) excess air coefficient 1.03, (**b**) excess air coefficient 1.05, (**c**) excess air coefficient 1.07, (**d**) excess air coefficient 1.09

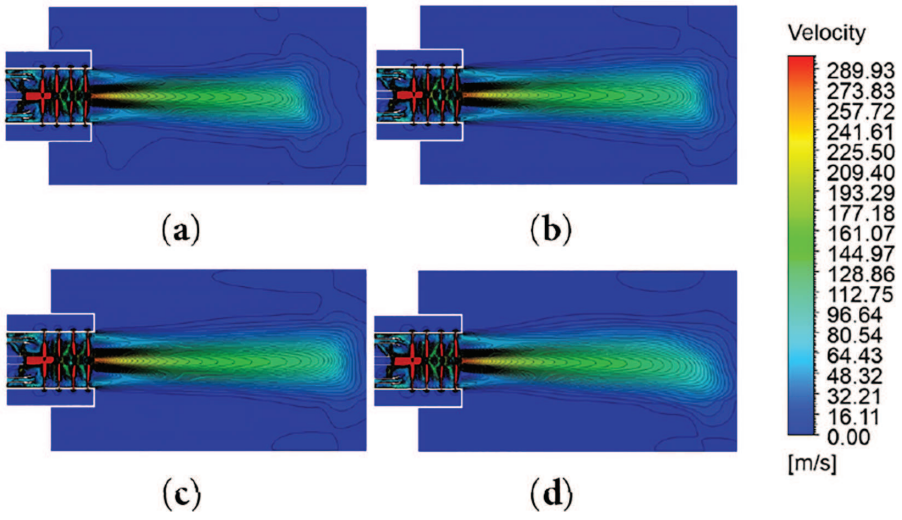


Figure 19: Velocity contours across different excess air coefficients. (**a**) excess air coefficient 1.03, (**b**) excess air coefficient 1.05, (**c**) excess air coefficient 1.07, (**d**) excess air coefficient 1.09

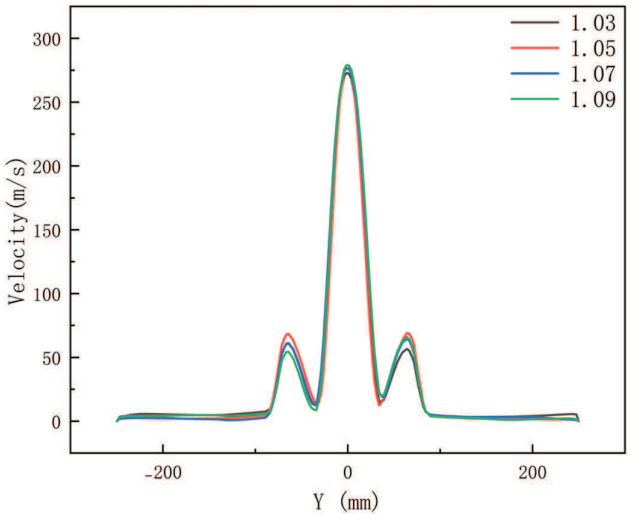


Figure 20: Velocity distribution profiles across different excess air coefficients

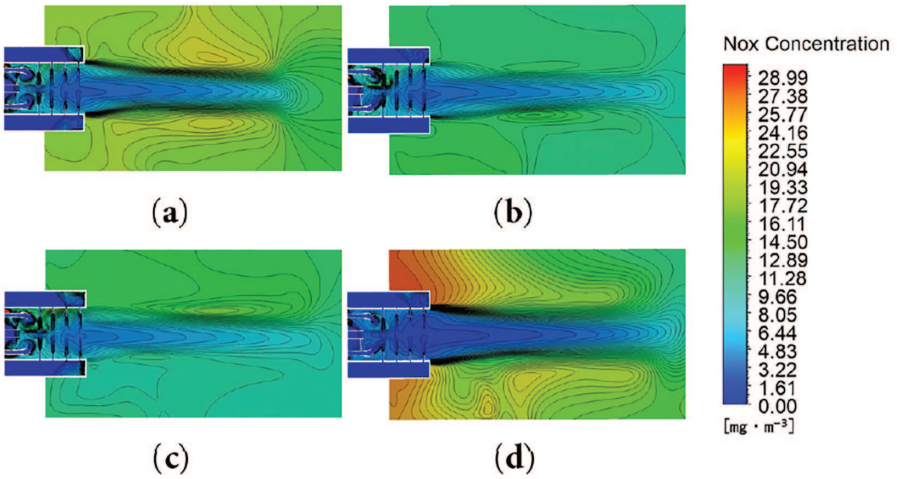


Figure 21: NOx concentration contours across different excess air coefficients. (**a**) excess air coefficient 1.03, (**b**) excess air coefficient 1.05, (**c**) excess air coefficient 1.07, (**d**) excess air coefficient 1.09

3.4 Influence of Air Preheating Temperature

In this study, the swirl impact gas burner was treated as the baseline case to examine the effect of preheated air temperature on its low-NOx combustion performance. Simulation conditions were set with the burner operating at full load, the cyclone blade deflection angle fixed at 20°, four nozzles in the main combustion stage, a primary-to-secondary air ratio of 2:8, and an excess air coefficient of 1.05. Within this operating framework, four inlet-air preheating temperatures, 300, 400, 500 and 600 K, were analyzed in order to assess their influence on the temperature distribution, flow characteristics and NOx emissions.

Fig. 22 presents the temperature distribution within the furnace chamber under various inlet air preheating conditions. It is observed that with rising preheating temperature, the dark red region expands, and the overall temperature increases significantly. Higher preheating levels reduce the distinction of the flame surface during staged combustion and enlarge the spatial extent of local high temperature regions. The effect of air preheating on the combustion process is expressed in two principal aspects. First, hot air

delivers greater enthalpy to the chamber, which accelerates fuel drying and combustion reactions. Second, it raises the kinetic energy of the incoming flow, strengthens turbulence, and promotes more effective mixing of fuel with air. The simulations show that at 300 K inlet temperature the flame remains relatively compact, whereas increasing the preheating temperature up to 600 K causes the flame core and surrounding high-temperature regions to merge and the high-temperature zone to expand markedly. Although preheating enhances the initial reaction rate and peak temperatures, the associated increase in radiative heat losses from the hottest regions and the higher propensity for local overheating partially offset the theoretical efficiency gains; in contrast, the 300 K case exhibits a more moderate temperature distribution that represents a practical compromise between energy utilization and thermal loading of the furnace walls.

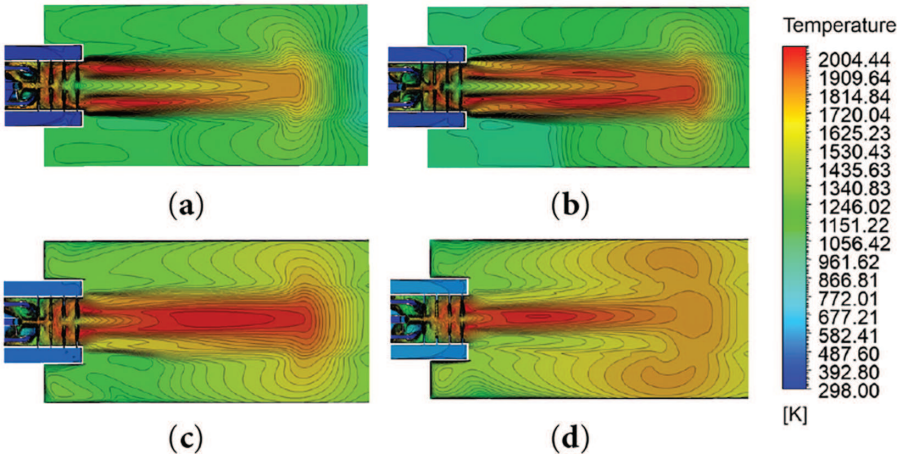


Figure 22: Temperature contours at different preheated air temperatures. (**a**) Preheating air temperature 300 K, (**b**) Preheating air temperature 400 K, (**c**) Preheating air temperature 500 K, (**d**) Preheating air temperature 600 K

Figs. 23 and 24 illustrate the velocity distributions at different air preheating temperatures and along the interface z = 257 mm, respectively. With increasing preheating temperature, the density of the incoming air decreases and the momentum exchange in the near-burner region is modified, leading to a gradual reduction in the mean flow velocity at the burner outlet and within the furnace for the operating conditions considered. At the same time, the elevated furnace temperature enhances turbulence intensity in the flow field, although the overall pattern of the velocity distribution remains essentially unchanged across the examined preheating levels. The lowest total flow velocity occurs at a preheating temperature of 600 K compared with other conditions.

Fig. 25 illustrates a contour plot of NOx concentration under various air preheating conditions. As the preheated air temperature rises, NOx levels increase noticeably, and the growth pattern is nearly linear. This behavior occurs because NOx formation is concentrated in high-temperature regions, and its generation rate is strongly influenced by thermal conditions. At 300 K inlet temperature, the NOx concentration reaches its minimum value of about 19.3 $mg \cdot m^{-3}$. When the preheated temperature rises to 400 K, the concentration increases to approximately 29 $mg \cdot m^{-3}$, and further preheating continues to raise NOx, although all cases remain within the regulatory limit for the present study. Among all cases, 300 K corresponds to the lowest NOx concentration within the combustion chamber. Hence, although preheating the inlet air enhances combustion efficiency, a relatively low preheating temperature (around 300 K) is considered the most suitable option when emission reduction goals are prioritized for this burner.

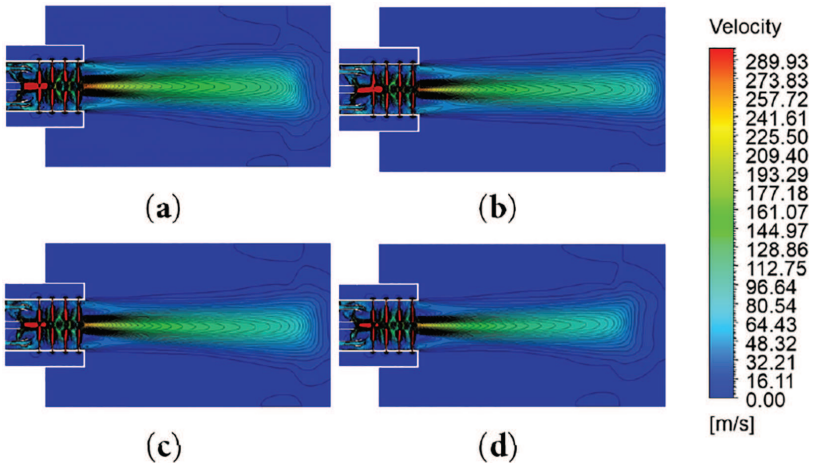


Figure 23: Velocity contours at different preheated air temperatures. (**a**) Preheating air temperature 300 K, (**b**) Preheating air temperature 400 K, (**c**) Preheating air temperature 500 K, (**d**) Preheating air temperature 600 K

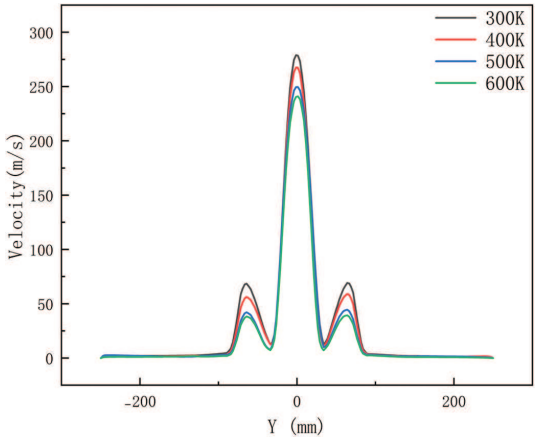


Figure 24: Velocity distribution profiles at different preheated air temperatures for interface z = 257 mm

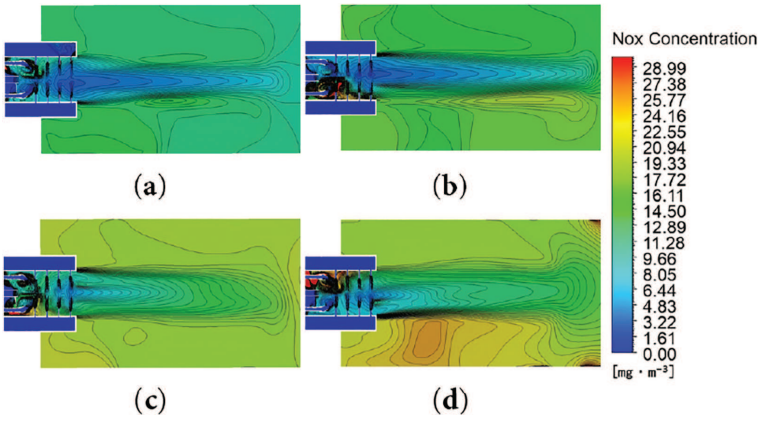


Figure 25: NOx concentration contours at different preheated air temperatures. (**a**) Preheating air temperature 300 K, (**b**) Preheating air temperature 400 K, (**c**) Preheating air temperature 500 K, (**d**) Preheating air temperature 600 K

4 Conclusion

The research examines grid independence and validates the computational model of the burner. Numerical simulations are employed to analyze how different operating conditions affect the furnace thermal field, flow field, and NOx concentration distribution, and to determine the optimal operational parameters for a cyclonic impingement natural-gas burner integrating four rows of impinging secondary-air tubes and four axially deflected main fuel nozzles. The main conclusions are summarized as follows:

(1) As the load increases, the furnace exhibits a larger high-temperature region, higher centerline temperature, and increased flow velocity, accompanied by localized backflow near the outlet. Improved mixing from the secondary air promotes more complete combustion. Benefiting from the combined swirl-impingement-staging arrangement, NOx levels rise with the temperature but still remain below 50 $mg{\cdot}m^{-3}$ across all conditions, indicating robust ultra-low-NOx performance under variable load.

(2) Increasing the primary-to-secondary air ratio initially raises the average furnace temperature and then reduces it, while NOx concentration increases overall. The highest average temperature occurs at a primary-to-secondary air ratio of 2:8, whereas the lowest NOx concentration is observed at a ratio of 1:9. Taking overall performance into account, and considering both combustion intensity and NOx emissions, a primary to secondary air ratio of 2:8 is considered optimal for the present burner geometry.

(3) As the excess air ratio increases, additional air at ambient temperature that does not participate directly in combustion enters the furnace. The average chamber temperature and NOx levels exhibit a non-monotonic trend: when the excess air coefficient increases from 1.03 to 1.05, improved mixing and moderated peak temperatures reduce thermal NOx most effectively, whereas further increases in excess air begin to raise NOx again. Considering combustion efficiency, an excess air coefficient of 1.05 is determined to be optimal.

(4) Higher air preheating temperatures increase the average temperature in the furnace chamber, which leads to a proportional rise in NOx concentration. Although preheating improves combustion efficiency, operating with approximately ambient-temperature air (≈300 K) provides the best compromise between emission reduction and energy consumption for the present swirl-impingement–staging burner.

Overall, these results confirm that the proposed structurally integrated burner, operated at a primary-to-secondary air ratio of 2:8, an excess air coefficient of about 1.05 and moderate air preheating, can achieve stable combustion with ultra-low NOx emissions and offers a practical design reference for compact industrial gas-fired systems.

Acknowledgement: Not applicable.

Funding Statement: This paper was supported by Postgraduate Research & Practice Innovation Program of Jiangsu Province (Project No.: SJCX24_1699).

Author Contributions: The authors confirm contribution to the paper as follows: study conception and design: Zhenjie Yuan; data collection: Zhenjie Yuan; analysis and interpretation of results: Zhenjie Yuan and Hailong Yu; case study: Hongjun Cao; draft manuscript preparation: Zhenjie Yuan. All authors reviewed the results and approved the final version of the manuscript.

Availability of Data and Materials: The data presented in this study are available on request from the corresponding author.

Ethics Approval: Not applicable.

Conflicts of Interest: The authors declare no conflicts of interest to report regarding the present study.

Symbols

ρ	Density ($kg \cdot m^{-3}$)
t	Time (s)
μ	Dynamic viscosity (Pa·s)
λ	Thermal conductivity ($W \cdot m^{-1} \cdot K^{-1}$)
β	Conserved scalar constructed from elemental mass fractions of C, H and N
u	Local streamwise velocity component ($m \cdot s^{-1}$)
y	Wall-normal dinormal distance measured from the inner furnacestance measured from the inner furnace wall toward the centerline (mm)
P	Static pressure (Pa)
Q	Fuel volumetric flow rate ($m^3 \cdot h^{-1}$)
R	Furnace radius (mm)
Z	Mixture fraction

Nomenclature

C_P	Specific heat at constant pressure ($J \cdot kg^{-1} \cdot K^{-1}$)
f_i	Body force per unit mass ($m \cdot s^{-2}$)
x_i	Spatial coordinate (i = 1, 2, 3) (m)
x_j	Spatial coordinate (j = 1, 2, 3) (m)
u_j	Velocity component in the j-direction ($m \cdot s^{-1}$)
u_i	Velocity component in direction i ($m \cdot s^{-1}$)
τ_{ij}	Stress tensor (Pa)
w_s	Source term coefficient ($kg \cdot m^{-3} \cdot s^{-1}$)
Q_S	Heat release per unit mass ($J \cdot kg^{-1}$)
q_v	Volumetric heat release (kcal)
U_{bulk}	Bulk (cross-sectional average) velocity at the corresponding axial location ($m \cdot s^{-1}$)
Z_C	Elemental mass fraction of carbon in the gas mixture
Z_H	Elemental mass fraction of hydrogen in the gas mixture
Z_N	Elemental mass fraction of nitrogen in the gas mixture
Z_{st}	Stoichiometric mixture fraction
β_f	Value of β in the pure fuel stream
β_{ox}	Value of β in the pure oxidiser stream

Abbreviations

DO	Discrete Ordinates
ULN	Ultra-low-NOx
CFD	Computational fluid dynamics
RANS	Reynolds-Averaged Navier-Stokes

References

1. Yu H, Jia X, Niu Y, Zhang Y. TSMS-InceptionNeXt: a framework for image-based combustion state recognition in counterflow burners via feature extraction optimization. Comput Mater Contin. 2025;83(3):4329–52. doi:10.32604/cmc.2025.061882.
2. Shingan B, Timung S, Jain S, Singh VP. Technological horizons in natural gas processing: a comprehensive review of recent developments. Sep Sci Technol. 2024;59(10–14):1216–40. doi:10.1080/01496395.2024.2366914.
3. García AM, López Y, Amell AA. Numerical analysis of oxygen enrichment in a self-recuperative radiant-tube burner. Int J Heat Mass Transf. 2024;223:125154. doi:10.1016/j.ijheatmasstransfer.2023.125154.

4. Ali G, Zhou Y. A detailed numerical analysis of NO_x formation and destruction during MILD combustion of CH_4/H_2 blends using a skeletal mechanism. Int J Hydrogen Energy. 2025;103:119–31. doi:10.1016/j.ijhydene.2025.01.149.
5. Jiang N, Chen B, Xu W, Cheng J, Tang Y, Zhu Y, et al. Flexible ligands enhance the high-performance synthesis of MIL-101-Cys 2 and its impact on greenhouse gas capture. J Environ Chem Eng. 2025;13(2):115960. doi:10.1016/j.jece.2025.115960.
6. Lu W, Liu Y, Zhang L, Liu F, Wu J, Zhan Z, et al. Flow and heat transfer characteristics of a new coke oven gas Ascension pipe heat exchanger: experimental validation and numerical study. Therm Sci Eng Prog. 2025;60:103386. doi:10.1016/j.tsep.2025.103386.
7. Zhao Y, Zhu X, Wang L, Gou J, Yan S, Liu X, et al. Study on the flame structure and combustion dynamics of ammonia swirl flame assisted by gliding arc plasma. Energy. 2025;340(1):139254. doi:10.1016/j.energy.2025.139254.
8. Li N, Chen Y, Jiang J, Zhang B, Sui C, Kong W. Effect of water vapor addition on the combustion characteristics in partially premixed swirling ammonia/methane/air flames. Int J Hydrogen Energy. 2025;128:10–21. doi:10.1016/j.ijhydene.2025.04.186.
9. Zhien CY, Ali Al-attab K. Design optimization of trio concept combustor geometry for low-grade biomass producer gas combustion. Energy. 2022;238:121705. doi:10.1016/j.energy.2021.121705.
10. Lei X, Lu H, Chang X, Zhou E. Numerical simulation of the influence of gear-type combustion stabilizer on the flow field distribution and combustion products of swirl burner. Case Stud Therm Eng. 2024;55:104078. doi:10.1016/j.csite.2024.104078.
11. Shao D, Zhong H, Wei X, Zhang J, Sun H, Han P, et al. Experimental study on NOx generation and emission characteristics of layer combustion of peanut shell briquette fuel. Bioresour Technol. 2026;440:133507. doi:10.1016/j.biortech.2025.133507.
12. Zeng G, Zhou A, Fu J, Ji Y. Experimental and numerical investigations on NOx formation and reduction mechanisms of pulverized-coal stereo-staged combustion. Energy. 2022;261:125358. doi:10.1016/j.energy.2022.125358.
13. Huang H, Xue X, Liu Y, Zhao J, Tian M, Niu Y. Numerical studies of a water-cooled premixed burner for low NOx combustion of natural gas. J Energy Inst. 2024;114:101647. doi:10.1016/j.joei.2024.101647.
14. Rezaeimanesh M, Asghar Ghoreyshi A, Peyghambarzadeh SM, Hassan Hashemabadi S. A coupled CFD simulation approach for investigating the pyrolysis process in industrial naphtha thermal cracking furnaces. Chin J Chem Eng. 2022;44:528–42. doi:10.1016/j.cjche.2021.03.028.
15. Pinto BM, Pacheco GP, Mendes MAA, Coelho PJ. Numerical simulation of natural gas/hydrogen combustion in a novel laboratory combustor. Appl Sci. 2025;15(13):7123. doi:10.3390/app15137123.
16. Manatunga M, Christo FC, Schlüter J, Shelyag S. Evaluating the steady flamelet assumption: impacts on flame structure and NO emissions in hydrogen/air turbulent jet diffusion flames. Combust Sci Technol. 2025;1–23. doi:10.1080/00102202.2025.2526448.
17. Jiang J, Yu Z, Weng W, Yang W, Liu S, He Y, et al. Experimental study and kinetic analysis of laminar burning velocity and temperature/OH/NO profiles of adiabatic NH_3/CH_4/air premixed flames combining heat flux burner and UV absorption spectroscopy. Combust Flame. 2026;283:114550. doi:10.1016/j.combustflame.2025.114550.
18. Arumugaraj S, Kumar P. Performance analysis of radiation heat transfer models for a kerosene fueled can combustor. Int J Therm Sci. 2026;221:110502. doi:10.1016/j.ijthermalsci.2025.110502.
19. Liu Y, Zhao Y, Zhang L, Wu J, Feng J, Zhou C, et al. Experiment and numerical study on combustion characteristics of low-nitrogen burners. Fuel. 2023;351:128814. doi:10.1016/j.fuel.2023.128814.
20. Sekar M, Alahmadi TA, Nithya S. Numerical simulation of industrial gas burners fueled with hydrogen-methane mixtures for enhanced combustion efficiency and reduced greenhouse gas emissions. Fuel. 2024;370:131807. doi:10.1016/j.fuel.2024.131807.
21. Amiri M, Barański J, Stasiak K, Ziółkowski P, Ditaranto M, Wiseman S, et al. Innovative oxy-fuel burner design with direct water injection for enhanced combustion control. Appl Therm Eng. 2025;281:128700. doi:10.1016/j.applthermaleng.2025.128700.

22. Xiao J, Liu Q, He S, Wang S, Zhang Z. Numerical simulation on combustion characteristics of methane/hydrogen blended fuel for non-premixed conical bluff body burner. Int J Hydrogen Energy. 2024;65:50–60. doi:10.1016/j.ijhydene.2024.03.377.
23. Fan H, Zhang H, Zhang X, Luo Z, Shao J, Liu H, et al. Experimental and numerical study of combustion and emission characteristics of biomass gasification gas blended with natural gas in a non-premixed burner. Renew Energy. 2026;256:123971. doi:10.1016/j.renene.2025.123971.